Journal of
Materials Chemistry A

ROYAL SOCIETY
OF CHEMISTRY

PAPER

View Article Online
View Journal

Check for updates

Cite this: DOI: 10.1039/d6ta03228a

Low loading thin film *vs.* industrially relevant powder electrodes as catalysts for anion exchange membrane water electrolysis

Karuppasamy Dharmaraj, *[a] Aline Alencar Emerenciano,[a] Can Kaplan,[a] Thorsten Schultz,[bc] Marcel Handke,[d] Norbert Koch, [bc] Rutger Schlatmann, [d] Iver Lauermann [d] and Michelle P. Browne *[a]

Received 16th April 2026
Accepted 8th June 2026

DOI: 10.1039/d6ta03228a

rsc.li/materials-a

Anion Exchange Membrane (AEM) electrolysers are currently classed as a lower technological readiness level for green H_2 production compared to maturer H_2 technologies such as proton exchange membrane and solid oxide electrolysers. This is due to a multitude of reasons including catalyst performance. To overcome this, new catalyst configurations must be understood and compared to the relevant industrial route, *i.e.*, powder deposition and materials, *i.e.*, nickel based. Herein, we report the advantages of thin film Ni magnetron sputtered catalysts for green H_2 production compared to commercially available NiO powder as a catalyst. The thin film catalysts show significantly improved performances in both a conventional three electrode setup and in an AEM device. Our results indicate that the thin films maintain exceptional structural stability, with near-edge X-ray absorption fine structure (NEXAFS) showing electronic activation primarily through surface sites without significant bulk structural reorganisation, as confirmed by extended X-ray absorption fine structure (EXAFS). In contrast, powder NiO catalysts display strong structural–electronic coupling with progressive structural changes paralleling NEXAFS evolution. In the zero-gap AEM electrolyser, Distribution of Relaxation Times (DRT) analysis further demonstrates that the bottleneck reaction is the oxygen evolution reaction with thin-film NiO exhibiting lower charge transfer resistance than powder NiO.

1. Introduction

Green hydrogen (H_2) production through water electrolysis generates a potential alternative to fossil fuels for the future energy transition.[1] In Germany, the National Hydrogen Strategy targets 10 GW of electrolyser capacity by 2030 and anticipates hydrogen demand reaching 400–800 TWh by 2050, supported by 18.9 billion euros in infrastructure investments and international import partnerships.[2] Adding this, the European Union's REPowerEU plan aims to produce and import 10 million tons of renewable hydrogen annually by 2030, fostering innovation through initiatives like IPCEIs and the Clean Hydrogen Partnership to achieve net-zero emissions by 2050.[3] Green H_2 is produced on the cathode in a water electrolyser which is called the Hydrogen Evolution Reaction (HER). However, the reaction on the opposite electrode (anode) is the bottleneck. On the anode, O_2 is produced, and this reaction is called the Oxygen Evolution Reaction (OER). There are three low temperature water electrolyser technologies that are either fully commercialised or in a stage of research and development to make green H_2: Alkaline Water Electrolysis (AWE), Anion Exchange Membrane (AEM) electrolysis and Proton Exchange Membrane (PEM) electrolysis. The latter two technologies are zero-gap electrolysers that utilise a membrane permeable to OH^- and H^+ ions, respectively, while AWE uses a diaphragm to separate the OER and HER and is more susceptible to gas crossover.[4]

Among the various electrolysis technologies, AEM water electrolysis is advantageous over AWE as AEM uses low OH^- concentration solutions (*e.g.*, neutral or 1 M) compared to higher OH^- solutions in AWE (5 M). Furthermore, AEM utilises non-noble metal catalysts, in contrast to PEM electrolysis technology that uses platinum group metals (PGMs), *e.g.*, IrO_2.[5] The state-of-the-art catalysts for the OER in AEMs are based on nickel, iron, and cobalt as reported in the literature.[6–11] Among the non-noble transition metals, nickel-based catalysts exhibit

---

[a] Helmholtz Young Investigator Group Electrocatalysis: Synthesis to Devices, Helmholtz-Zentrum Berlin für Materialien und Energie GmbH, Hahn-Meitner-Platz 1, 14109 Berlin, Germany. E-mail: michelle.browne@helmholtz-berlin.de; karuppasamy.dharmaraj@helmholtz-berlin.de

[b] Joint Research Group Hybrid Material Systems, Helmholtz-Zentrum Berlin für Materialien und Energie GmbH, Brook-Taylor-Straße 6, 12489 Berlin, Germany

[c] Institut für Physik & CSMB, Humboldt-Universität zu Berlin, Zum Großen Windkanal 2, 12489 Berlin, Germany

[d] Institute Competence Centre Photovoltaics Berlin, Helmholtz-Zentrum Berlin für Materialien und Energie GmbH, Schwarzschildstrasse 3, 12489 Berlin, Germany

high performances for the OER in alkaline environments.[12,13] Ni and NiO catalysts are known for industrial applications and show high electrocatalytic activity and stability for alkaline electrolysis at the industrial scale. Ni based catalysts can be synthesised *via* various methods, including solvothermal synthesis, electrodeposition, thermal decomposition, sol–gel methods, gas–solid reactions and electro-reductive synthesis.[14–17] Typically, catalysts in the powder form are widely prepared using one of these methods, then mixed with solvents such as alcohol and/or water and coated onto gas diffusion electrodes (GDEs) using coating techniques including spray coating.[18] These powder catalysts often require polymeric binders to adhere well on the conductive substrates and to improve the electrical conductivity of the catalyst to the substrate.[18] However, optimal binder content is critical for excellent catalytic activity in electrolyser devices.[19,20] A significant challenge in catalyst preparation is scaling up production to large quantities while maintaining uniform catalyst distribution and reproducibility, particularly for large geometric areas of the substrates. Hence, inhomogeneous catalyst distribution remains a key limitation.

In general, physical deposition methods such as thermal evaporation, arc evaporation, pulsed laser deposition, electron beam evaporation, or sputtering could help overcome these coating challenges for electrodes. Magnetron sputtering, in particular, is a widely used industrial method for a variety of metallic and ceramic coatings. Complex coatings with a thickness range of less than a nanometer up to several hundred nanometers can be deposited very efficiently, reproducibly and with high uniformity on large areas. In the case of insulating target materials, radio-frequency sputtering is used to overcome the problem of target charging. Depositing catalysts at nanoscale thicknesses can significantly enhance the electrochemically active surface area, thereby improving electrocatalytic activity for water electrolysis. Sputtered catalysts can be directly deposited onto porous substrates, such as nickel foam or metallic GDEs (*e.g.*, nickel or titanium felts), enabling their use as catalyst-coated metal felts in zero-gap electrolysers. Furthermore, these sputtered thin films exhibit potential benefits by offering enhanced efficiency, durability, and stability for application in electrolyser devices over powder catalysts and improved selectivity towards products in organic molecule synthesis.[21–23]

In this study, we compare a commercially available NiO powder (p-NiO) catalyst with a magnetron-sputtered NiO thin-film (t-NiO) catalyst with ultra-low loading. The commercial powder catalyst was formulated into inks and spray-coated onto nickel fibre felt (NF) gas diffusion electrodes (GDEs). Both powder and thin-film catalysts were subjected to three-electrode electrochemical characterisation, followed by zero-gap AEM electrolyser testing of the best-performing catalyst over 60 hours of continuous operation at different current densities. The product H_2 at the cathode was continuously monitored. Post-mortem analyses were performed to elucidate the catalysts' physical and chemical changes after the electrolyser operation. Furthermore, *operando* X-ray absorption spectroscopy (XAS) was carried out from open-circuit potential (OCP) to the OER region to elucidate the chemical behaviour of both catalysts.

2. Results

2.1 Fabrication and characterisation of t-NiO and p-NiO

In order to optimise the intrinsic OER activity of the Ni based thin films prepared by magnetron sputtering before integrating into an AEM device, Ni films with various ultra-low thicknesses were prepared, Fig. 1a. Both powder and thin film NiOs were directly prepared on a high surface area industrially used metal porous nickel fibre felt gas diffusion layer (NF) (Fig. S1) with different t-NiO of thicknesses 5 nm, 10 nm, 15 nm and p-NiO of mass loading 1.0, 2.0, and 5.0 mg cm^{-2}. Scanning Electron Microscopy (SEM) analysis (Fig. 1b–e), combined with Energy Dispersive X-ray spectroscopy (EDX) elemental mapping confirmed changes in surface roughness and Ni–O composition. The p-NiO coating exhibited a heterogeneous surface, likely due to non-uniform or limited deposition, whereas the t-

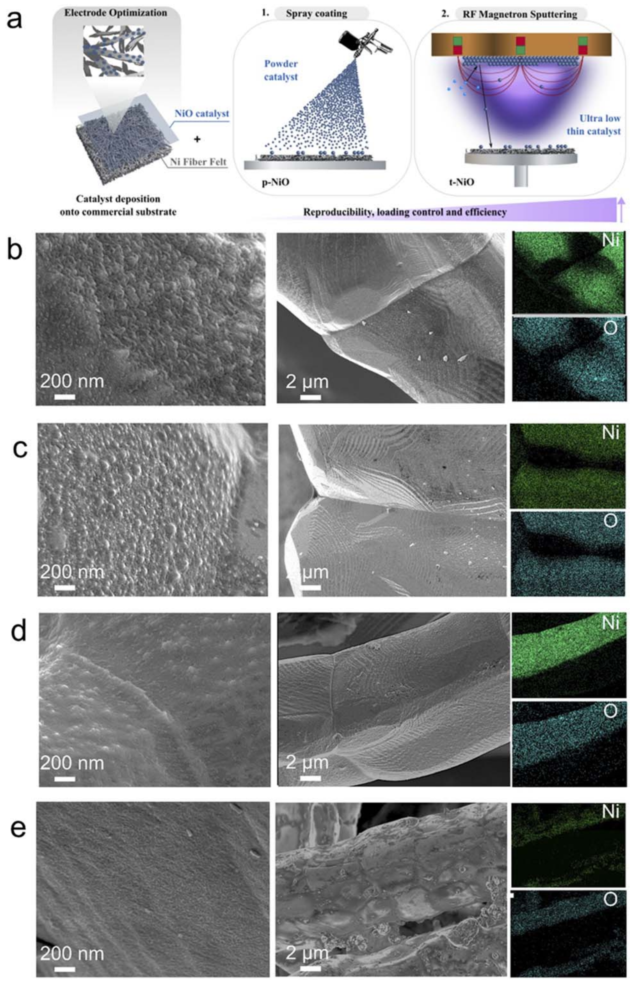

Fig. 1 (a) Schematic illustration of the preparation of sprayed and magnetron-sputtered NiO, scanning electron microscopy images of (b) 5, (c) 10, and (d) 15 nm thickness NiO magnetron-sputtered on NF and (e) sprayed NiO powder of 1.0 mg cm^{-2} loading.

NiO thin films displayed a more homogeneous and rougher morphology.[24,25] In t-NiO, the observed characteristic clusters were absent in bare Ni fibre felt (Fig. S1), and the surface roughness decreased as the sputtered Ni layer thickness increased. These observations suggest that the energetic ion beam used in sputtering modifies the microstructure of Ni fibers, promoting the growth of columnar grains with different crystallographic orientation and alignment. For p-NiO, the variation in surface roughness appears linked to increased film thickness, which may mask the columnar Ni grains and reduce the exposed surface area. From the linear sweep voltammograms (LSVs), the NiO film with 10 nm thickness, t-NiO (10 nm)/

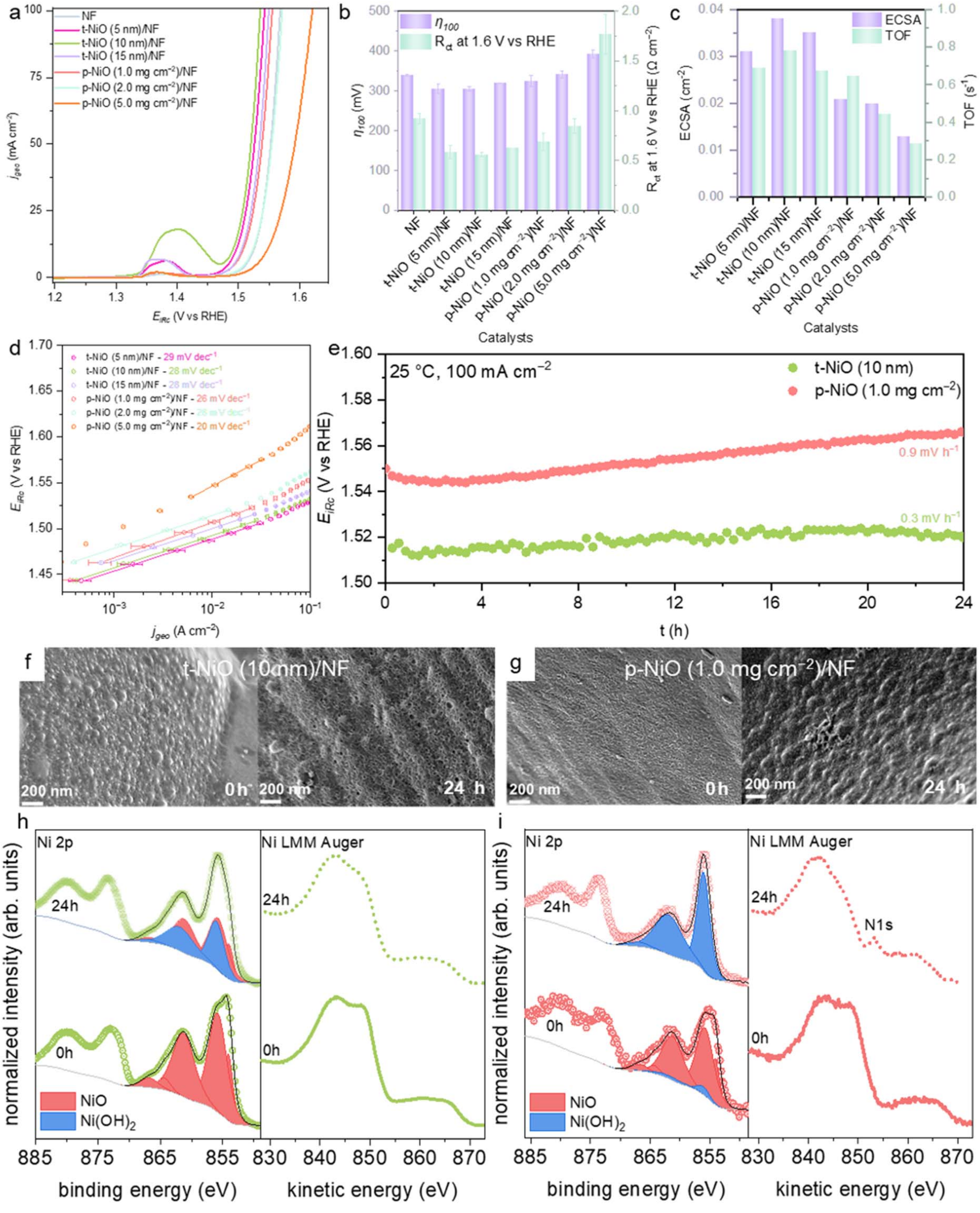

Fig. 2 Characterisation of t-NiO and p-NiO. (a) LSVs at 5 mV s^{-1}, (b) overpotential at 100 mA cm^{-2}, R_{ct} at 1.6 V, (c) ECSA, TOF, (d) Tafel slopes, (e) stability test at 100 mA cm^{-2}, (f and g) SEM images before and after stability tests, and (h and i) XPS spectra of Ni 2p and Ni LMM Auger spectra of t-NiO and p-NiO catalysts before and after the stability test.

NF showed the best activity and it required 1.53 V to reach 100 mA cm^{-2}, following the activity trend, t-NiO (10 nm)/NF > t-NiO (5 nm)/NF > t-NiO (15 nm)/NF > p-NiO (1.0 mg cm^{-2})/NF > NF > p-NiO (2.0 mg cm^{-2})/NF > p-NiO (5.0 mg cm^{-2})/NF (Fig. 2a). Furthermore, t-NiO (10 nm)/NF exhibits low charge transfer resistance (R_{ct}) in the OER region with a high electrochemical active surface area (ECSA) and turn over frequency (TOF) of 0.038 cm^{-2} and 0.8 s^{-1} compared to other prepared catalysts (Fig. 2b and c). The catalyst kinetics were evaluated through steady state chronoamperometry Tafel plots and powder catalysts show a slope of 20–28 mV dec^{-1} whereas all the three thin films exhibit about 28 mV dec^{-1} (Fig. 2d). These findings indicate that the NiO catalysts are governed by a rate-determining O_2 desorption step ($M{-}OOH + OH^- \rightarrow M + H_2O + O_2 + e^-$).[26,27] The stabilities of the best performing thin film (t-NiO (10 nm)/NF, from here on simply referred to as t-NiO) and powder (p-NiO (1.0 mg cm^{-2})/NF from here on simply referred to as p-NiO) catalysts were measured at constant current at 100 mA cm^{-2}. The chronopotentiogram shows that after 24 hours t-NiO (10 nm)/NF undergoes less catalyst degradation of 0.3 mV h^{-1} than p-NiO (1.0 mg cm^{-2})/NF which is about 0.9 mV h^{-1} (Fig. 2e). The NF substrate showed 15 mV higher overpotential with catalyst degradation of 0.9 mV h^{-1} than p-NiO (Fig. S2). Furthermore, R_{ct} at 100 mA cm^{-2} of t-NiO is the same after 24 h of stability operation (Fig. S3). This shows that t-NiO is quite stable maintaining the catalytically active sites compared to p-NiO. Morphological changes following 24-hour electrochemical stability tests are presented in Fig. 2f and g. p-NiO exhibited pronounced surface modifications, indicating the formation of a new oxidation layer and a substantial increase in carbon species, as verified by elemental mapping. The carbon deposition observed on p-NiO after long-term stability testing is likely attributed to the degradation of the ionomer binder used during electrode fabrication under prolonged anodic potentials. For the optimised electrodes, in addition to elevated carbon content, p-NiO showed significant surface alterations, including the emergence of clusters and a more heterogeneous morphology after the stability tests. These features may result from catalyst leaching during the tests and/or exposure of the underlying Ni fibres with formation of a hydroxide layer (Fig. S4). In contrast, the surface of the 10 nm thick sputtered electrode remained largely unchanged compared to its pre-test state. Furthermore, elemental mapping revealed a lower carbon content on these electrodes after stability testing. These findings suggest that the 10 nm Ni layer was preserved, which may contribute to the enhanced chemical stability of sputtered electrodes relative to those produced *via* powder deposition. The oxidation states of nickel in p-NiO and t-NiO before and after stability testing were analysed by X-ray photoelectron spectroscopy (XPS). The Ni 2p core level and Ni LMM Auger spectra are presented in Fig. 2h for t-NiO and Fig. 2i for p-NiO. For the pristine catalyst performance measurements (Fig. S5), the materials were deposited on graphite foil (GF) substrates to avoid spectral interference from the NF. The t-NiO sample exhibits two distinct Ni 2p peaks at 854.5 eV and 856.1 eV binding energy, characteristic of NiO, which is further corroborated by the Auger line shape with features at 843.2 eV and 848.0 eV kinetic energy.[28] In contrast, the Ni 2p spectrum of p-NiO appears broader, and the two characteristic NiO peaks are not well resolved, suggesting the presence of at least one secondary phase. To quantify the relative contributions of NiO and $Ni(OH)_2$, we applied the fitting procedure described by Biesinger *et al.*[29] NiOOH was not considered, as its characteristic Auger feature at 833 eV kinetic energy was absent.[28] The fitting results reveal that pristine t-NiO consists exclusively of NiO, while p-NiO already contains a minor fraction of $Ni(OH)_2$. After 24 h of stability testing, p-NiO is fully converted to $Ni(OH)_2$ (Fig. 2i), whereas the t-NiO sample retains ~60% NiO, highlighting the superior stability of t-NiO compared to p-NiO.

The catalytic activity was further assessed using a non-Ni-based substrate, GF to determine the intrinsic activities of sputtered thin film and powder NiOs. The detailed physical characterisation is shown in Fig. S5. The t-NiO (10 nm)/GF and p-NiO (1.0 mg cm^{-2})/GF were characterised for the OER in 1.0 M KOH electrolyte. LSVs (Fig. S6a) show that t-NiO (10 nm)/GF and p-NiO (1.0 mg cm^{-2})/GF require 1.61 V and 1.83 V *vs.* RHE respectively to achieve 10 mA cm^{-2}. The overpotentials at 10 mA cm^{-2} were obtained from the LSVs and are summarised in Fig. S6b. The p-NiO (1.0 mg cm^{-2})/GF requires *ca.* 200 mV higher overpotential to reach the 10 mA cm^{-2} than t-NiO (10 nm)/GF. The ECSA was determined, and it shows that t-NiO exhibits about 10 times larger active area than the p-NiO (1.0 mg cm^{-2})/GF (Fig. S6c). Furthermore, the number of redox active species of the t-NiO (10 nm)/GF is higher (Fig. S6c), which results in an increase in turn-over frequency compared to p-NiO (1.0 mg cm^{-2})/GF. This shows that t-NiO (10 nm)/GF possesses better OER activity compared to commercially available p-NiO (1.0 mg cm^{-2})/GF. The Nyquist plot at the OER region further confirms the lower electron transfer resistance for t-NiO (10 nm)/GF compared to p-NiO (1.0 mg cm^{-2})/GF (Fig. S6d). These electrochemical results conclude that thin films with ultra-low mass loading (~6.7 μg cm^{-2}) contain better electrochemical active sites combined with lower charge transfer resistance towards the alkaline OER compared to the p-NiO (1.0 mg cm^{-2})/GF.

2.2 *Operando* electrochemical characterisation of t-NiO and p-NiO

To elucidate the structural and electronic evolution of the catalysts under the reaction conditions, *operando* XAS measurements were performed (Fig. 3). *In situ* near-edge X-ray absorption fine structure (NEXAFS) spectroscopy was employed to investigate the electronic and structural evolution, while Fourier-transform Extended X-ray Absorption Fine Structure (EXAFS) spectra provided complementary insights into the local atomic arrangement and bond distances. NEXAFS and EXAFS spectra were acquired for both catalyst t-NiO/GF (Fig. 3a and b) and p-NiO/GF (Fig. 3c and d) under identical reaction conditions to enable direct comparison of their electronic and structural dynamics during catalysis. Fig. 3a and c display the NEXAFS spectra of t-NiO and p-NiO respectively. The Ni K-edge absorption energies were monitored as a function of applied potential to elucidate the oxidation state changes and structural

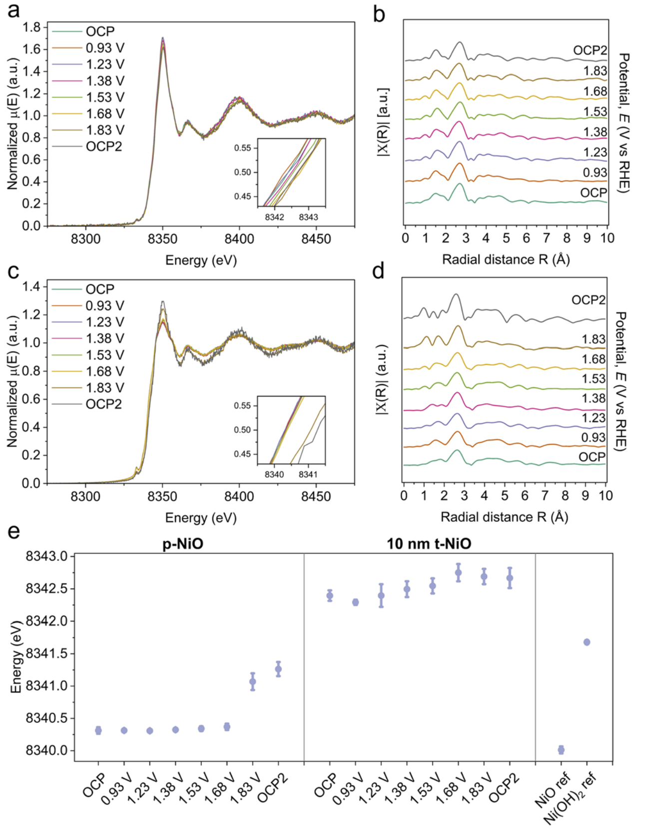

Fig. 3 *Operando* X-ray characterisation at various applied potentials (V *vs.* RHE, 0% *iR* correction) for t-NiO (10 nm)/GF and p-NiO (1.0 mg cm^{-2})/GF. (a) NEXFAS and (b) EXAFS spectra for t-NiO (10 nm)/GF and (c) NEXFAS and (d) EXAFS spectra for p-NiO (1.0 mg cm^{-2})/GF. (e) Edge energy spectra for both t-NiO (10 nm)/GF and p-NiO (1.0 mg cm^{-2})/GF.

transformations. The reference materials exhibited characteristic Ni K-edge positions at 8340.01 eV for NiO and 8341.7 eV for $Ni(OH)_2$, consistent with Ni^{2+} in octahedral coordination. The 1.7 eV difference reflected distinct coordination environments, with $Ni(OH)_2$ showing higher edge energy due to increased Ni–O bond covalency.[30–32] The t-NiO exhibited an initial edge energy of 8342.4 eV at OCP, approximately 2.4 eV above the bulk NiO reference (8340.0 eV). As pre-mortem XPS showed predominantly NiO with no significant $Ni(OH)_2$ or NiOOH surface species, this elevation likely arose from Madelung potential shifts and interfacial charge-transfer effects at the NiO/graphite interface rather than chemical oxidation. The asymmetric boundary conditions could create an electrostatic environment where Fermi level equilibration between NiO (band gap ~3.6 eV) and graphite (semi-metallic) causes electron delocalisation from NiO into the substrate. This renders the near-interface region slightly hole-doped with Ni^{3+}-like electronic character. NEXAFS, averaging over the 10 nm thickness, captured this interfacial gradient as an apparent edge upshift without chemical oxidation.[33,34] This interpretation is supported by studies on oxide thin film interfaces. Direct studies of NiO/graphene and NiO/reduced graphene oxide interfaces have demonstrated heterojunction formation with charge transfer and Fermi level equilibration, where the conducting carbon substrate acts as an electron donor to p-type NiO, creating apparent Ni^{3+} character through electronic modulation rather than chemical oxidation.[35–37] Furthermore, substrate electronic effects on XAS edge positions have been directly demonstrated in oxide thin films, where electron-withdrawing substrates shifted apparent oxidation states in XANES spectra without chemical transformation.[38] Resonant XAS studies of oxide heterostructures have confirmed that X-ray absorption spectroscopy is indeed sensitive to interfacial charge transfer and electronic structure reconstruction, validating our use of XANES to detect these interfacial electronic effects.[39] Upon applying potential, edge energy increased systematically from 8342.3 eV at 0.93 V to 8342.75 eV at 1.68 V, then decreased slightly to 8342.7 eV at 1.83 V before stabilising at 8342.7 eV at OCP2. This potential-dependent evolution of approximately 0.5 eV, superimposed on the Madelung-shifted baseline, indicated genuine surface oxidation. Post-mortem XPS confirmed mixed NiO/$Ni(OH)_2$ in approximately equal amounts, demonstrating partial surface transformation during the OER while preserving the bulk structure.

The p-NiO maintained approximately 8340.3 eV from OCP through 1.68 V, only slightly higher than the bulk NiO reference and consistent with pre-mortem XPS showing predominantly NiO. At 1.83 V, edge energy shifted dramatically to 8341.3 eV, indicating significant Ni oxidation and showing complete irreversibility upon returning to OCP2. Post-mortem XPS confirmed predominantly $Ni(OH)_2$, demonstrating extensive bulk transformation.

The 2.1 eV difference in initial edge energies indicated fundamentally different electronic structures with distinct origins. The p-NiO edge energy (8340.3 eV) reflected bulk Ni^{2+} character, while the 10 nm film elevation (8342.4 eV) likely arose from interfacial charge-transfer effects. p-NiO exhibited threshold behavior with minimal changes below 1.68 V followed by abrupt oxidation at 1.83 V, characteristic of bulk phase transition requiring substantial overpotential. In contrast, t-NiO showed gradual, continuous evolution, suggesting efficient activation where interfacial electronic pre-conditioning facilitated surface-confined oxidation at lower overpotentials.

Fourier-transform EXAFS spectra provided complementary insights into local structural changes accompanying the NEXAFS electronic transitions (Fig. 3b, d and S7). Radial distribution functions revealed distinct coordination environment evolution patterns for each morphology. The thin film showed exceptional structural stability throughout the entire potential range, with well-defined coordination shells at approximately 1.6 Å (first Ni–O shell) and 2.6 Å (second Ni–Ni shell) maintaining positions and intensities with minimal variations (Fig. 3b). The only notable change was a small peak emerging at approximately 1.1 Å from 0.93 V onwards, remaining constant throughout the potential series. This suggested a small portion of highly oxidised Ni sites with contracted Ni–O bonds, consistent with surface oxidation confirmed by post-mortem XPS (mixed NiO/$Ni(OH)_2$). The main coordination shells showed no splitting, broadening, or intensity changes, indicating that the majority of sites retained their original NiO coordination. At OCP2, the small 1.1 Å component persisted, indicating minor irreversible surface activation, though the overall coordination environment remained close to the initial state. This structural stability despite significant NEXAFS changes (continuous $\sim$0.5 eV edge evolution) confirmed the activation mechanism: (1) Madelung/interfacial effects providing electronic pre-conditioning without structural change, and (2) partial surface oxidation creating active sites while preserving bulk integrity. Contrasting the structural stability of the thin film, the powder NiO displayed complex, progressive structural evolution, correlating with the chemical transformation suggested by XPS (Fig. 3d). The initial spectrum showed a characteristic NiO rock salt structure with well-defined shells at approximately 1.6 Å and 2.6 Å. However, structural changes began above 1.38 V, with the first coordination shell showing incipient splitting that became progressively pronounced with increasing potential. From 1.38 V to 1.68 V, two components emerged: a shorter distance (approximately 1.1 Å) characteristic of Ni^{3+} species, and the original distance (approximately 1.65 Å) corresponding to residual Ni^{2+}–O bonds. At 1.83 V, both peaks achieved equal intensity, suggesting approximately 50% conversion. At OCP2, the evolution became more complex. The 1.65 Å peak split into components at approximately 1.45 Å and 1.9 Å, while the 1.1 Å peak shifted to approximately 0.9 Å. This restructuring suggested multiple distinct coordination environments formed during relaxation. The 0.9 Å component indicated extremely short Ni–O bonds, possibly terminal oxo species or highly distorted geometries characteristic of metastable oxyhydroxide phases while the 1.9 Å component might represent Ni–OH bonds or hydrated coordination environments. This structural memory effect demonstrated irreversible bulk activation, creating a complex mixture of coordination environments differing significantly from both initial and fully oxidised states. Post-mortem XPS showing predominantly $Ni(OH)_2$ validated this extensive transformation. The apparent discrepancy between the $\sim$50% Ni^{3+} conversion estimated from *operando* EXAFS at 1.83 V and the near-complete $Ni(OH)_2$ conversion observed by post-treatment XPS is consistent with the inherent differences between these techniques. EXAFS, measured in fluorescence mode, provides a bulk-averaged structural picture, whereas XPS probes only the outermost $\sim$5–10 nm of the material. Consequently, the surface of p-NiO likely undergoes more extensive transformation during operation than the bulk-averaged EXAFS signal reflects. Furthermore, upon removal from the electrochemical cell, residual NiO and partially oxidised intermediates undergo spontaneous hydroxylation under ambient conditions, driving the near-complete conversion to $Ni(OH)_2$ captured by post-treatment XPS. The progressive transformation from OCP into 1.83 V correlated excellently with NEXAFS evolution, while the OCP2 restructuring explained the elevated final edge energy.

In summary, EXAFS revealed striking differences in structural–electronic coupling. t-NiO exhibited remarkable structural stability despite significant continuous NEXAFS evolution, with only a subtle 1.1 Å peak appearance. Combined with XPS showing limited surface transformation, this suggests: (1) Madelung/interfacial effects providing electronic pre-conditioning without structural change, and (2) limited surface oxidation creating active sites while preserving bulk integrity. p-NiO on the other hand showed strong structural–electronic coupling with intense progressive changes concomitant with the NEXAFS evolution and XPS-confirmed transformation. Gradual first shell splitting from OCP through 1.83 V, culminating in equal peak intensities, demonstrated extensive bulk transformation involving approximately 50% of sites (Fig. 3e). The OCP2 restructuring, creating four distinct coordination environments, confirmed extensive irreversible bulk activation.

2.3 Zero-gap electrolyser tests

The catalysts' stability was evaluated in an in-house developed zero-gap 4.0 cm^{-2} flow field area electrolyser at 60 °C (Fig. S8) and the test rig is controlled by an in-house made LabVIEW-based software.[40] The schematic representation of zero-gap AEM electrolyser operation is shown in Fig. 4a. The anode consisted of either t-NiO (10 nm)/NF or p-NiO (1.0 mg cm^{-2})/NF, with Pt-coated carbon paper as the cathode. Catalysts were activated post-assembly using multiple current steps, as detailed in Table S1, before measuring the current–voltage (*I–V*) curves. The mass normalised *I–V* curves show that t-NiO (10 nm)/NF delivers a current density of 150 mA cm^{-2}, whereas p-NiO (1.0 mg cm^{-2})/NF reaches only 0.8 mA cm^{-2} at 2.1 V, corresponding to an approximately 188-fold higher activity (Fig. 4b). Consistently, the geometric area-normalized *I–V* curves indicate that t-NiO (10 nm)/NF requires 2.1 V to achieve 1.0 A cm^{-2}, while p-NiO (1.0 mg cm^{-2})/NF requires an additional 78 mV (Fig. 4c). Both catalysts were tested at current densities of 0.1, 0.5, and 1.0 A cm^{-2} for 65 hours each (Fig. 4d). At 1.0 A cm^{-2}, t-NiO (10 nm)/NF exhibited an initial cell voltage of about 2.0 V, increasing by 150 mV over time, with minimal voltage degradation over 120 h. The cell voltage for t-NiO (10 nm)/NF was slightly lower than that for the p-NiO (1.0 mg cm^{-2})/NF catalyst. Bare porous NF is active for water electrolysis which showed a cell voltage 170 mV higher than catalyst coated NF. At 0.5 A cm^{-2}, t-NiO (10 nm)/NF exhibited a cell voltage 80 mV lower than p-NiO (1.0 mg cm^{-2})/NF. Furthermore, at a very low current density of 0.1 A cm^{-2}, both thin films and powder NiO catalysts showed similar cell voltages, indicating comparable active sites and performance at low current densities. At high current densities, the TOF of t-NiO was significantly higher than that of p-NiO, outperforming the p-NiO catalyst. The high frequency resistance (HFR) and H_2 production rates were continuously monitored (Fig. 4e and f). HFR revealed higher ohmic losses at low current densities, with minimal losses and lower resistance at high current densities. Extended operation showed that low-loading sputtered t-NiO film performed comparably to the powder Ni catalysts. The mass normalised H_2 production flow rate of t-NiO (10 nm)/NF is 142 times higher than that of p-NiO (1.0 mg cm^{-2})/NF, reaching about 1000 ml min^{-1} mg^{-1} *versus* 7 ml min^{-1} mg^{-1} at 1.0 A cm^{-2}. Both catalysts achieved an electrolyser cell efficiency of 58% and an energy consumption of about 60 kWh kg^{-1} at 1.0 A cm^{-2} (SI Note 1, Table S2). Electrochemical impedance spectroscopy (EIS) was conducted at current densities of 50 and 100 mA cm^{-2}, revealing lower charge transfer resistance for thin films compared to

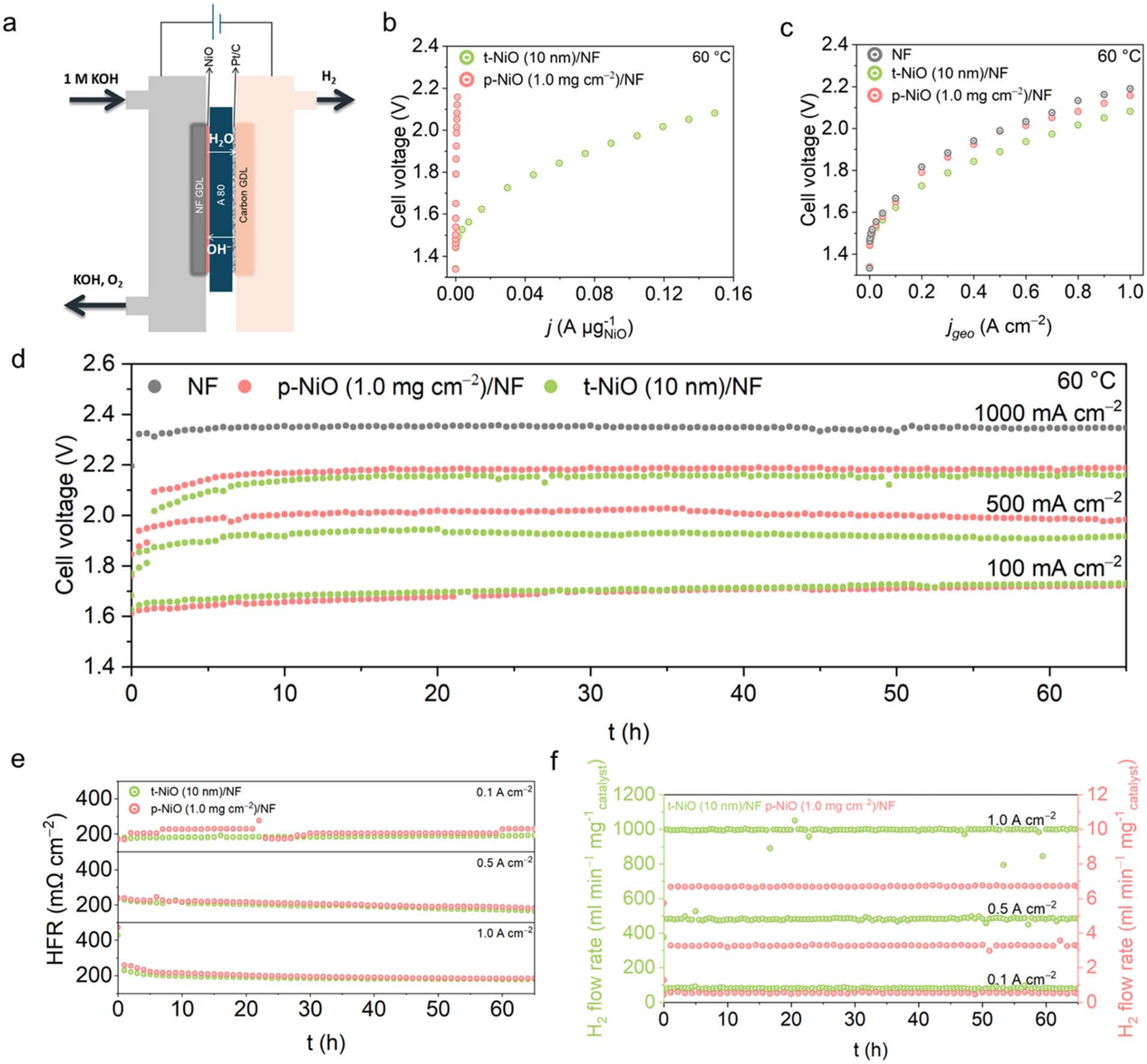

Fig. 4 (a) Schematic representation of the zero-gap electrolyser, (b and c) steady state mass normalised I–V curves, (d) chronopotentiogram of electrolyser tests at various current densities, (e) HFR measured during electrolyser operation, and (f) H_2 production rate normalised to catalyst mass loading.

powder NiO catalysts (Fig. 5a and S9). The EIS data were further analysed using the distribution of relaxation times (DRT). The linear Kramers–Kronig transform test confirmed measurement validity with residuals less than 1% (Fig. S10). The parameters of the DRT are provided in Table S3. Fig. 5b shows the DRT spectra of the full electrolyser cell, measured at 50 and 100 mA cm^{-2}, which displays five distinct peaks: P_1 (<0.8 Hz, mass transport), P_2 (5–12 Hz, OER), P_3 (43–500 Hz, HER), P_4 and P_5 (>500 Hz, ionic transport in catalyst layers) consistent with the literature.[41] Comparison of P_2 and P_3 indicates that cell overpotentials are dominated by OER charge transfer at the anode, with faster HER kinetics due to Pt at the cathode. Increasing the current density shifts the OER peak (P_2) to slightly higher frequencies, consistent with observations by Trattner *et al.*[41]^{6} Furthermore, the P_2 peak area for t-NiO (10 nm)/NF was smaller than that for p-NiO (1.0 mg cm^{-2})/NF and bare NF.

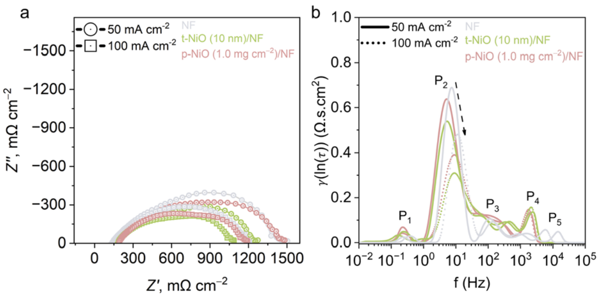

Fig. 5 Current density dependence of (a) Nyquist plots and (b) DRT spectra for the electrolyser cell.

Postmortem analysis of anodes after 65 h of electrolyser tests distinctly reveals different surface morphologies between t-NiO/NF and p-NiO/NF electrodes. SEM images (Fig. 6a and b) show

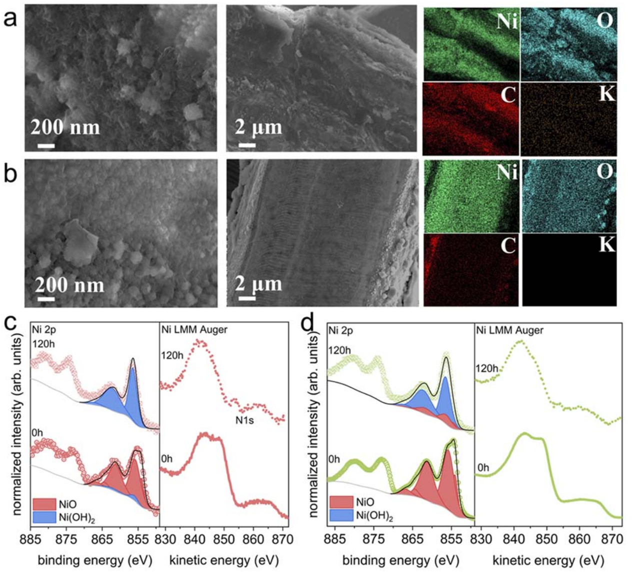

Fig. 6 Post-characterisation after 60 h of electrolyser tests. (a) SEM images and EDX mapping of p-NiO (1.0 mg cm^{-2})/NF, (b) SEM images and EDX mapping of t-NiO (10 nm)/NF and (c and d) Ni 2p and Ni LMM Auger XPS spectra for both catalysts before and after testing.

a clearly heterogeneous layer with irregular agglomerates on the p-NiO/NF surface. In contrast, the t-NiO/NF electrode displays a more uniform surface with only minor grain agglomeration along the edges. This indicates that the ultra-thin sputtered Ni layer maintains greater chemical stability under real test conditions, exhibiting a lower accumulation of impurities such as carbon and hydroxides that can improve stability, as confirmed by EDX analysis. Furthermore, the lateral particle agglomeration observed on the sputtered thin catalyst suggests increased exposure of the substrate surface during testing. Fig. 6c and d display the XPS spectra of the pristine p-NiO and t-NiO samples prior to and following 65 h of stability testing. After 65 h, residual NiO can still be detected in the t-NiO sample, whereas the p-NiO sample is fully converted to Ni(OH)$_2$, consistent with the transformation already observed after 24 h.

3. Discussion of the enhanced activity of thin film NiO over powder NiO

This study demonstrates the superior electrocatalytic performance of thin-film NiO catalysts compared to their powder-based counterparts for the OER in zero-gap electrolysers. The t-NiO catalysts, particularly the 10 nm films, exhibit a higher TOF and lower overpotential in three-electrode measurements, alongside an exceptional electrolyser efficiency of 64% at a current density of 500 mA cm^{-2}, with sustained H_2 production for over 60 hours. The enhanced performance of t-NiO can be attributed to its optimised physicochemical properties (Fig. 7). The thin-film morphology provides a higher surface area and uniform roughness structure ensuring robust stability under both short- and long-term electrochemical conditions. In contrast, p-NiO suffers from heterogeneity, surface degradation, cluster formation, catalyst leaching, and significant impurity accumulation, which collectively compromise its stability and durability. Table S4 compares the AEM electrolyzer results of this work with recently reported noble metal-free OER catalysts under similar operating conditions, demonstrating that the sputtered t-NiO/NF anode achieves competitive cell performance comparable to thin-film and nanostructured catalysts.

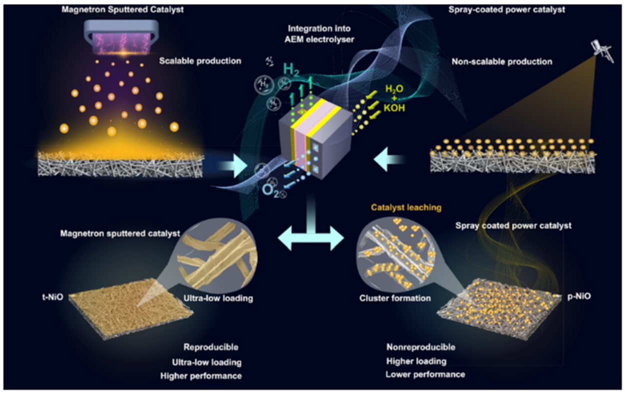

Fig. 7 Schematic illustration comparing the t-NiO and p-NiO catalysts.

Operando NEXAFS and EXAFS analyses provide deeper insights into the mechanistic origins of t-NiO's superior performance. The 10 nm t-NiO film exhibits a higher initial edge energy (8342.4 eV) compared to p-NiO (8340.31 eV), indicative of an electronic pre-conditioning resulting from Madelung potential shifts and interfacial charge-transfer from the NiO/graphite interface pre-existing higher oxidation states that facilitate OER activity without requiring extensive electrochemical activation. Furthermore, the t-NiO film demonstrates a continuous increase in edge energy across the potential range, reflecting an efficient electronic activation mechanism that maximises active site utilisation. In contrast, p-NiO requires significantly higher overpotentials for activation, with a gradual edge energy increase up to 1.68 V, followed by a sharp shift (+0.7 eV) at 1.83 V, suggesting an inefficient, threshold-dependent activation process. This disparity underscores the ability of t-NiO to achieve rapid and effective activation, enhancing its catalytic efficiency. Structural stability is another critical factor distinguishing t-NiO from p-NiO. The 10 nm t-NiO film maintains exceptional framework integrity, with only subtle emergence of catalytically active 1.1 Å sites, balancing the generation of active species with structural preservation. Conversely, p-NiO undergoes extensive structural disruption, including progressive splitting and approximately 50% bulk conversion, which may compromise long-term catalyst stability and performance.

Beyond the intrinsic physicochemical differences between t-NiO and p-NiO, the performance gap is further widened by structural constraints inherent to the powder electrode preparation. Spray-coating of p-NiO onto the NF produces a non-uniform distribution of active material, resulting in local variations in catalyst layer thickness, particle aggregate size, and the formation of dense, cracked regions that impede both ionic and electronic transport. As demonstrated for analogously prepared electrodes, such morphological inhomogeneity reduces reactant accessibility to active sites and leads to suboptimal overall catalyst utilisation, whereas controlled deposition methods yielding homogeneous and porous catalyst layers significantly improve active site accessibility and electrochemical performance.[42] In addition, the presence of Nafion ionomer as a binder in p-NiO introduces a further constraint on electrochemically accessible surface sites. Although Nafion provides mechanical stability and ionic conductivity to the catalyst layer, its sulfonate (SO_3) functional group has been shown to adsorb more strongly on NiO than the key OER intermediate OH*, effectively blocking active Ni sites and promoting competing side reactions including sulfate and bisulfate formation that suppress OER kinetics.[43] These electrode-level limitations act cumulatively with the intrinsic powder morphology constraints, collectively amplifying the performance difference observed between p-NiO and t-NiO.

The t-NiO films demonstrate enhanced catalytic activity, characterised by higher turnover frequency, lower overpotential, and an efficient electronic activation mechanism driven by pre-existing higher oxidation states and well-distributed active sites. Additionally, their structural stability ensures long-term durability, with minimal degradation even under prolonged electrochemical conditions. In contrast, p-NiO suffers from high activation barriers, bulk structural instability, and possess irreversible changes. The thin-film architecture significantly enhances electrode active area while minimizing catalyst loading, offering a compelling cost-performance advantage over powder-based catalysts. By addressing key limitations such as heterogeneity, surface degradation, and impurity accumulation, t-NiO presents a scalable and reproducible strategy for industrial-scale water electrolysis. These findings underscore the transformative potential of thin-film catalysts in advancing the efficiency, sustainability, and economic viability of green hydrogen production, paving the way for the development of next-generation electrocatalysts for electrolyser technologies.

4. Conclusions

In conclusion, NiO thin films (10 nm) prepared by magnetron sputtering on industrially relevant nickel felt exhibited significantly higher electrochemically active sites than conventional powder NiO catalysts (1.0 mg cm^{-2}). Combined *operando* XAS and *ex situ* XPS analyses revealed fundamentally different activation mechanisms for morphologically distinct NiO catalysts. The sputtered thin film demonstrated an energetically favorable two-component mechanism where Madelung potential shifts and interfacial charge-transfer from the NiO/support interface likely elevated the baseline edge energy without chemical oxidation, while fractional surface oxidation during cycling created active sites while preserving bulk integrity. This structural–electronic decoupling enabled continuous NEXAFS evolution despite exceptional EXAFS stability, with post-mortem XPS confirming mixed NiO/$Ni(OH)_2$ surface composition. In contrast, the powder exhibited strong structural–electronic coupling requiring extensive bulk transformation, with progressive reorganization involving approximately 50% of sites directly paralleling NEXAFS changes and post-mortem XPS showing predominantly $Ni(OH)_2$. In zero-gap AEM electrolyser tests, the thin film NiO anode demonstrated stable operation with a hydrogen production rate 140 times higher than that of powder NiO, despite using significantly less catalyst material. DRT analysis confirmed the higher intrinsic activity of thin films, attributed to lower charge transfer resistance compared to powder NiO. Overall, the use of low-loading NiO thin films offers a scalable approach for high-performance, industrially viable AEM electrolysers.

5. Experimental section

5.1 Chemicals and materials

Powder nickel oxide (Ni(II)O, 99.99% metal basis) and potassium hydroxide pellets (KOH, EMPLURA) were obtained from Sigma Aldrich and Merck respectively. 5 wt% Nafion (Quintech), isopropanol (≥98% Technical, VWR Chemicals), 25 wt% HCl (for analysis EMSURE, Merck), and acetone (≥99% Technical, VWR Chemicals) were used in this study. The electrolytes and catalyst inks were prepared from a Barnstead Smart2Pure Pro deionised (DI) water system from Thermo Scientific. Nickel fiber felt (NF, 35 μm fiber diameter, 0.5 mm thickness, 80% porosity) from Xinxiang Aida Machinery Equipment Corporation, China was used as the high surface area metal gas diffusion layer substrate. Flexible graphite foil (GF, 99.8% purity, 0.075 mm thickness) was used as the non-Ni substrate. PiperION™-A80-HCO3 from Versogen was used as the anion exchange membrane. N_2 (5N) from Airliquide was used.

5.2 Preparation of powder NiO (p-NiO) catalysts

For the preparation of the powder NiO catalyst, the inks were prepared and sprayed using a spraying gun (Harder & Steenbeck Airbrush) connected with N_2 (1.5 bar pressure). During catalyst spraying, the metal fibre substrates were held at 80 °C on a hot plate (IKA® C-Mag hotplate stirrers). The inks contain NiO powder, isopropanol (IPA), DI water and 5 wt% Nafion. The IPA to DI water is 3 : 1 (vol%) and Nafion to catalyst is 8 μl $mg_{catalyst}^{-1}$.

5.3 Preparation of thin film (t-NiO) catalysts

NiO (10 nm) was deposited *via* an in-vacuum radio frequency magnetron sputtering process (Planarmagnetron, ION'X-3UHV_9102; Thin Film Consulting, D-72661 Grafenberg) from a NiO target (99.9% purity, Nova Fabrica) in a pure Ar (99.999%) atmosphere. The sputtering process was conducted at a power of 60 W, pressure of $(5.2 \pm 0.1) \times 10^{-3}$ mbar, a constant sputtering bias of (210 ± 3) V, a distance of ≈ 5 cm between the target and sample, and for a duration of 34 s.[44]

5.4 Physical characterisation

A Zeiss MERLIN Scanning Electron Microscope (SEM) with a 0.1–30 keV field emission gun was used to examine the electrocatalysts' morphologies at an accelerating voltage of 4 kV.

Elemental mapping regions were imaged using Transmission Electron Microscopy (TEM, FEI Titan 80–300, Thermo Fisher Scientific) combined with an Energy Dispersive X-ray Spectroscopy (EDS, Bruker XFlash 6–30) detector. X-ray photoelectron spectroscopy measurements (XPS) were conducted with a JEOL JPS-9030 setup, using a non-monochromated Mg Kα excitation source and a hemispherical analyser with a pass energy of 30 eV, yielding an overall energy resolution of 1.2 eV. The samples exhibited charging, so the binding energy scale was shifted such that the adventitious carbon peak is located at 285.0 eV. CasaXPS was used for fitting the spectra, using Shirley backgrounds and GL(50) line shapes for all peaks.[45] Raman spectra were recorded using an i-Raman Plus spectrometer from BWTEK, using a laser 785 nm excitation source. 25% of the laser power was used for all measurements. The spectra were collected for 100 seconds with two average integration times.

5.5 Electrochemical characterisation

All the three electrode measurements were carried out in a Zennium E4 potentiostat. Hg/HgO filled with 1.0 M KOH (ALS Co., Ltd) as the reference electrode, graphite rod as the counter electrode (Redoxme) and catalyst coated NF or GF as the working electrode were used. All the measured potentials against Hg/HgO were converted into Reversible Hydrogen Electrode (RHE) potential (HydroFlex from Gaskatel GmbH, Germany), by measuring the open circuit potential in N_2 saturated 1.0 M KOH electrolyte ($E_{\mathrm{RHE}} = E_{\mathrm{Hg/HgO}} + 0.924$). Prior to the catalyst coating on the NF, the NF was cleaned with 25% HCl, DI water, acetone, isopropyl alcohol, and DI water in an ultrasonication bath each for 10 minutes. Linear sweep voltammograms (LSVs) were recorded at 5 mV s^{-1}. For the Tafel slopes, chronoamperometry at various increment potentials was used. The potentials were applied for at least 30 s and the mean of the last 5 seconds were used for plotting the Tafel plots. Potentiostatic electrochemical impedance spectroscopy (EIS) was conducted from 200 kHz to 100 mHz with 10 mV amplitude at fixed potential *vs.* RHE. Galvanostatic EIS was collected from 200 kHz to 100 mHz with 10% of applied currents (minimum 5 mA cm^{-2}) as the amplitude. Before EIS measurements, the respective currents or potentials were applied to reach the steady state. The electrochemical active surface area (ECSA) was calculated using the double layer capacitance method, with cyclic voltammograms at scan rates 25, 50, 100, and 200 mV s^{-1} in the potential window −0.2 to 0.2 V *vs.* Hg/HgO (1.0 M KOH). Average non-faradaic current density, $\Delta j = (j_a - j_c)/2$, where j_a and j_c are anodic and current currents calculated at 0 V *vs.* Hg/HgO (1.0 M KOH). The obtained slope (F) from scan rates *vs.* Δj was divided by a specific capacitance value of 40 μF to obtain ECSA. The turnover frequency (TOF) was calculated using the following equation, $j/4Q$, where j is the current density measured at potential 1.55 V *vs.* RHE, the factor 4 denotes the number of electrons transferred per molecule of oxygen produced and Q is the voltametric charge density obtained from the Ni oxide cathodic peak. All reported electrode potentials were subjected to full (100%) *iR* correction.

5.6 *Operando* measurements

X-ray absorption spectroscopy (XAS) measurements were performed at the SAMBA beamline at SOLEIL synchrotron, France. Working electrodes (WEs) were prepared by drop-casting a dispersion of catalyst material onto a flexible graphite foil (GF) support, followed by drying on a hot plate at 60 °C. For sputtered samples, a 10 nm NiO thin film was deposited onto the GF by sputtering. The XAS measurements were conducted in a custom-built three-electrode cell equipped with the as-prepared WE, a Pt wire counter electrode (CE), and an Hg/HgO (filled with 1.0 M KOH) reference electrode (RE). Fluorescence spectra were collected at a 45° angle relative to the WE surface at the Ni K-edge. Energy calibration was performed using Ni metal foil as the reference. Typically, *ex situ* XAS spectra of catalysts and references were initially obtained for the samples in the three-electrode cell. Subsequently, the cell was filled with N_2-purged 1.0 M KOH, and XAS spectra were collected at the open circuit potential (OCP). Chronoamperometry measurements were then performed at successive potentials of 0, 0.3, 0.45, 0.6, 0.75 V and 0.9 *vs.* Hg/HgO, with XAS spectra collected during each potential step. Finally, the samples were characterised again at OCP. Data analysis was conducted using the software Fastosh v1.0.9.[46] The edge positions in the X-ray absorption near-edge structure (XANES) spectra were determined using the half-edge step method.[47]

5.7 Zero-gap electrolyser tests

The zero-gap electrolyser tests were conducted using a ZAHNER ZENNIUM PRO potentiostat coupled with a PP211 booster. The testing protocol is detailed in Table S1. An in-house developed cell with 4.0 cm^2 geometric flow field area (2.0 cm × 2.0 cm) made up of stainless steel was used for the electrolyser test. A Bronhorst mass flow controller (EL-FLOW Select, 100 ml min^{-1}) was used for measuring the produced H_2. A silica gel column (Merck Supelco, granulate, orange gel (1–3 mm)) was used before the mass flow controller inlet to trap the moisture. The electrolyte flow rate was controlled at 25 ml min^{-1} using a BT600L Intelligent Flow Peristaltic Pump (two channels) and delivered to the anode, while the cathode was kept dry. A temperature controller (LTR 2500) from Juchheim GmbH & Co. KG, tubing (A-60-G, (I.D. = 4.3 mm, O.D. = 6 mm)) from Tygon® and a heating mat (cylindrical 138 W + 200 °C, ø 115 mm, 240 V ac) from RS PRO were used for the electrolyser tests. The electrolyte inlet temperature to the cell is ensured to be at 60 °C. Pt coated H23C6 carbon paper (0.5 mg cm^{-2}) from Quintech was used as the cathode. A Piperion A80 membrane was used as the AEM. The A80 membrane was activated by soaking in N_2 saturated 1.0 M KOH for at least 24 h. Polytetrafluoroethylene (PTFE) gaskets, with a thickness of 0.5 and 0.3 mm, were used as both anode and cathode gaskets respectively. A torque of 3.5 Nm was applied to the electrolyser cell in a zigzag pattern, incrementally increased in 0.5 Nm steps. Chronopotentiometry at different current densities measured for each 30 seconds and mean value of 5 seconds were used for the SS polarisation curve. For high frequency resistance (HFR) measurements, galvanostatic electrochemical impedance spectroscopy (GEIS) spectra were recorded between 200 kHz and 1 kHz at respective fixed currents with an amplitude of 10% of absolute applied currents (minimum 5 mA cm^{-2}). The HFR, representing the cell's ohmic resistance, is determined from the initial *x*-axis intercept of the impedance spectrum.

The distribution of relaxation times (DRT) was extracted using open-source software published by F. Ciucci *et al.*, enabling the transformation of experimental electrochemical impedance spectroscopy (EIS) spectra into time-domain information.[48] The DRTtools Python package was employed.[49] Eqn (1) describes a series resistance (R_s) connected in series with an infinite number of parallel RC elements. The function $\gamma(\ln(\tau))$ represents the distribution of total polarisation resistance across the relaxation time scale, as described by eqn (2).

$$Z_{\mathrm{DRT}}(\omega) = R_s + \int_{-\infty}^{\infty} \frac{\gamma(\ln(\tau))}{1+i\omega\tau}\mathrm{d}\ln\tau \qquad (1)$$

$$\int_{-\infty}^{\infty} \gamma(\ln(\tau))\mathrm{d}\ln\tau = R_{\mathrm{pol}} \qquad (2)$$

For the DRT analysis, the parameters listed in Table S3 were used. Before the DRT analysis and EIS fitting, the EIS data were validated using the linear Kramers–Kronig (KK) transform test to confirm causality, linearity and the time invariance.[50] The Lin-KK tool (version 1.3 (16.12.2015)) was used to fit EIS spectra and calculate residuals.[51] The KK transforms relate the real and imaginary components of the impedance spectrum for a linear, time-invariant, and causal system, as described by eqn (3) and (4).

$$Z'(\omega) = Z'(\infty) + \frac{2}{\pi}\int_0^{\infty} \frac{xZ''(x) - \omega Z''(\omega)}{x^2-\omega^2}\mathrm{d}x \qquad (3)$$

$$Z''(\omega) = -\frac{2\omega}{\pi}\int_0^{\infty} \frac{Z'(x) - Z'(\omega)}{x^2-\omega^2}\mathrm{d}x \qquad (4)$$

where $Z'(\omega)$ and $Z''(\omega)$ represent the real and imaginary components of the impedance, respectively, as a function of frequency, ω.

Conflicts of interest

There are no conflicts to declare.

Data availability

The data that support the findings of this study are available from the corresponding author upon reasonable request.

Supplementary information (SI): additional experimental details, characterization results and electrochemical measurements supporting the main findings. See DOI: https://doi.org/10.1039/d6ta03228a.

Acknowledgements

We gratefully acknowledge the Helmholtz Association's Initiative and Networking Fund (Helmholtz Young Investigator Group VH-NG-1719) and the support from the German Federal Ministry of Education and Research in the framework of the project Catlab (03EW0015A/B) for the funding. The authors acknowledge support from the Federal Ministry of Research, Technology and Space (BMFTR) in the framework of the project ASCEND (03SF0798A). The authors would like to particularly thank Dr Florian Ruske from the Microscopy Corelabs of the Helmholtz Zentrum Berlin for providing access to their facility and training on the equipment. Open Access funding was enabled and organised by Projekt DEAL. K. D. and M. P. B. acknowledge Iris Dorbandt and Maximilian Reinhardt for logistical assistance with the electrolyser setup. We acknowledge SOLEIL for provision of synchrotron radiation facilities, and we would like to thank Dr Andrea Zitolo for assistance in using beamline SAMBA under proposal 20241245. We also thank Dr Thomas Rossi at Helmholtz Zentrum Berlin for valuable discussion during the XAS analysis.

References

1 A. M. Oliveira, R. R. Beswick and Y. Yan, *Curr. Opin. Chem. Eng.*, 2021, **33**, 100701.

2 *Hydrogen Economy in Germany*, https://www.gtai.de/en/invest/industries/energy/green-hydrogen, accessed August 04, 2025.

3 *European Commission EU's Energy System*, https://energy.ec.europa.eu/topics/eus-energy-system/hydrogen_en, accessed August 4, 2025.

4 J. Kraakman, Master, Eindhoven University of Technology, 2023.

5 T. B. Ferriday, S. N. Sampathkumar, P. H. Middleton, M. L. Kolhe and J. Van Herle, *Int. J. Energy Res.*, 2024, **2024**, 1–28.

6 A. Erbe, M. F. Tesch, O. Rüdiger, B. Kaiser, S. Debeer and M. Rabe, *Phys. Chem. Chem. Phys.*, 2023, **25**, 26958–26971.

7 H. Li, Y. Zhang, Y. Chen, Y. Li, Z. Li, B. Yang, Q. Zhang, J. Lu, L. Lei, Z. J. Xu and Y. Hou, *Angew. Chem., Int. Ed.*, 2025, **64**(8), e202423071.

8 A. Moysiadou and X. Hu, *J. Mater. Chem. A*, 2019, **7**, 25865–25877.

9 Y. Zheng, W. Ma, A. Serban, A. Allushi and X. Hu, *Angew. Chem., Int. Ed.*, 2025, **64**(1), e202413698.

10 K. W. Ahmed, M. J. Jang, S. Habibpour, Z. Chen and M. Fowler, *Electrochem*, 2022, **3**, 843–861.

11 D. Xu, M. B. Stevens, M. R. Cosby, S. Z. Oener, A. M. Smith, L. J. Enman, K. E. Ayers, C. B. Capuano, J. N. Renner, N. Danilovic, Y. Li, H. Wang, Q. Zhang and S. W. Boettcher, *ACS Catal.*, 2019, **9**, 7–15.

12 Y. Chen, K. Rui, J. Zhu, S. X. Dou and W. Sun, *Chem.–Eur. J.*, 2019, **25**, 703–713.

13 S. Guo, Q. Lu, X. Zhou, Y. Wang, M. Li and B. Liu, *Energy Fuels*, 2025, **39**, 7915–7940.

14 G. Schröder, S. Sajjadi, B. Schmiedecke, A. A. Emerenciano, T. Schultz, N. Koch, M. Buldu-Akturk and M. P. Browne, *ChemElectroChem*, 2025, **12**(9), e202400656.

15 P. B. Michelle, H. Nolan, N. C. Berner, G. S. Duesberg, P. E. Colavita and M. E. G. Lyons, *Int. J. Electrochem. Sci.*, 2016, **11**, 6636–6647.

16 K. Dharmaraj, R. Hanna, I. Lauermann, R. Bagacki, F. Xi, E. Kemppainen, R. Schlatmann and S. Calnan, *ACS Sustain. Chem. Eng.*, 2024, **12**, 9908–9921.

17 K. Dharmaraj, R. Hanna, F. Ruske, D. Douglas-Henry, I. Lauermann, S. Prathapani, P. Reyes-Figueroa, Y. Rodriguez-Ayllon, Y. Lu, V. Nicolosi, R. Schlatmann, M. P. Browne, P. W. Menezes and S. Calnan, *Chem. Eng. J.*, 2025, **522**, 167192.

18 C. Kaplan, K. Dharmaraj, T. Schultz, L. Qin, N. Chen, D. A. Douglas-Henry, B. Schmiedecke, M. Buldu-Akturk, A. Zuber, I. Dorbandt, M. Reinhardt, Y. Rodriguez-Ayllon, Y. Lu, V. Nicolosi, N. Koch, J. Rosen and M. P. Browne, *Adv. Funct. Mater.*, 2026, **36**(21), 2503842.

19 E. K. Volk, A. L. Clauser, M. E. Kreider, D. D. Soetrisno, S. Khandavalli, J. D. Sugar, S. Kwon and S. M. Alia, *ACS Electrochem.*, 2025, **1**, 239–248.

20 J. Hyun, S. H. Yang, D. W. Lee, E. Oh, H. Bae, M. S. Cha, G. D. d, J. Y. Lee and H.-T. Kim, *Chem. Eng. J.*, 2023, **469**, 143919.

21 Z. Li, E. Öztuna, K. Skorupska, O. V. Vinogradova, A. Jamshaid, A. Steigert, C. Rohner, M. Dimitrakopoulou, M. J. Prieto, C. Kunkel, M. Stredansky, P. Kube, M. Götte, A. M. Dudzinski, F. Girgsdies, S. Wrabetz, W. Frandsen, R. Blume, P. Zeller, M. Muske, D. Delgado, S. Jiang, F.-P. Schmidt, T. Köhler, M. Arztmann, A. Efimenko, J. Frisch, T. M. Kokumai, R. Garcia-Diez, M. Bär, A. Hammud, J. Kröhnert, A. Trunschke, C. Scheurer, T. Schmidt, T. Lunkenbein, D. Amkreutz, H. Kuhlenbeck, V. J. Bukas, A. Knop-Gericke, R. Schlatmann, K. Reuter, B. R. Cuenya and R. Schlögl, *Nat. Commun.*, 2024, **15**, 10660.

22 E. López-Fernández, J. Gil-Rostra, J. P. Espinós, A. R. González-Elipe, F. Yubero and A. d. Lucas-Consuegra, *J. Power Sources*, 2019, **415**, 136–144.

23 P. Kúš, *Thin-film Catalysts for Proton Exchange Membrane Water Electrolyzers and Unitized Regenerative Fuel Cells*, Springer, 2019.

24 A. M. Reddy, A. S. Reddy, K.-S. Lee and P. S. Reddy, *Solid State Sci.*, 2011, **13**, 314–320.

25 J. Xu, T. Shao, S. Wei and L. Qin, *Surf. Coat. Technol.*, 2010, **204**, 3443–3450.

26 O. Van Der Heijden, R. E. Vos and M. T. M. Koper, *ACS Energy Lett.*, 2025, **10**, 3040–3049.

27 R. Chen, G. Sun, C. Yang, L. Zhang, J. Miao, H. Tao, H. Yang, J. Chen, P. Chen and B. Liu, *Nanoscale Horiz.*, 2016, **1**, 156–160.

28 M. C. Biesinger, L. W. Lau, A. R. Gerson and R. S. C. Smart, *Phys. Chem. Chem. Phys.*, 2012, **14**, 2434–2442.

29 M. C. Biesinger, B. P. Payne, L. W. Lau, A. Gerson and R. S. C. Smart, *Surf. Interface Anal.*, 2009, **41**, 324–332.

30 W. O'grady, K. Pandya, K. Swider and D. Corrigan, *J. Electrochem. Soc.*, 1996, **143**, 1613.

31 K. Pandya, R. Hoffman, J. McBreen and W. O'Grady, *J. Electrochem. Soc.*, 1990, **137**, 383.

32 S. Lee, Y.-C. Chu, L. Bai, H. M. Chen and X. Hu, *Chem Catal.*, 2023, **3**, 100475.

33 I. Preda, A. Gutiérrez, M. Abbate, F. Yubero, J. Méndez, L. Alvarez and L. Soriano, *Phys. Rev. B:Condens. Matter Mater. Phys.*, 2008, **77**, 075411.

34 P. S. Bagus, C. J. Nelin, X. Zhao, S. V. Levchenko, E. Davis, X. Weng, F. Späth, C. Papp, H. Kuhlenbeck and H.-J. Freund, *Phys. Rev. B*, 2019, **100**, 115419.

35 G. Xin, F. Liu, T. Ju, Y. Cheng, J. Bao, W. Sun, J. Song and C. Bulin, *Chem. Eng. J.*, 2025, **513**, 162863.

36 C. Tang, L. Zhong, R. Xiong, Y. Xiao, B. Cheng and S. Lei, *J. Colloid Interface Sci.*, 2023, **648**, 181–192.

37 S. S. Niavol, M. Budde, A. Papadogianni, M. Heilmann, H. M. Moghaddam, C. M. Aldao, G. Ligorio, E. J. List-Kratochvil, J. M. J. Lopes and N. Barsan, *Sens. Actuators, B*, 2020, **325**, 128797.

38 M. J. Powell, I. J. Godfrey, R. Quesada-Cabrera, D. Malarde, D. Teixeira, H. Emerich, R. G. Palgrave, C. J. Carmalt, I. P. Parkin and G. Sankar, *J. Phys. Chem. C*, 2017, **121**, 20345–20352.

39 Y. Cao, X. Liu, M. Kareev, D. Choudhury, S. Middey, D. Meyers, J.-W. Kim, P. Ryan, J. Freeland and J. Chakhalian, *Nat. Commun.*, 2016, **7**, 10418.

40 R. Bagacki, M. Reinhardt, R. Schlatmann, S. Calnan, R. Van De Krol and M. P. Browne, *Chem. Commun.*, 2025, **61**, 10210–10227.

41 M. Ranz, B. Grabner, B. Schweighofer, H. Wegleiter and A. Trattner, *J. Power Sources*, 2024, **605**, 234455.

42 I. Fouzai, M. Radaoui, S. Díaz-Abad, M. A. Rodrigo and J. Lobato, *ACS Appl. Energy Mater.*, 2022, **5**, 2138–2149.

43 M.-A. Ha, E. K. Volk, O. Leitner, A. Isakov, H. J. González Vélez, S. Alia and R. Larsen, *ACS Electrochem.*, 2025, **1**, 1339–1351.

44 I. Lauermann and A. Steigert, *Journal of Large-Scale Research Facilities JLSR*, 2016, **2**, A67.

45 N. Fairley, V. Fernandez, M. Richard-Plouet, C. Guillot-Deudon, J. Walton, E. Smith, D. Flahaut, M. Greiner, M. Biesinger, S. Tougaard, D. Morgan and J. Baltrusaitis, *Appl. Surf. Sci. Adv.*, 2021, **5**, 100112.

46 G. Landrot and E. Fonda, *Synchrotron Radiation*, 2025, p. 32.

47 J. Wang, C.-S. Hsu, T.-S. Wu, T.-S. Chan, N.-T. Suen, J.-F. Lee and H. M. Chen, *Nat. Commun.*, 2023, **14**(6576).

48 T. H. Wan, M. Saccoccio, C. Chen and F. Ciucci, *Electrochim. Acta*, 2015, **184**, 483–499.

49 *pyDRTtools*, https://github.com/ciuccislab/pyDRTtools.

50 M. Schönleber, D. Klotz and E. Ivers-Tiffée, *Electrochim. Acta*, 2014, **131**, 20–27.

51 *Kramers-Kronig Validity Test Lin-KK for Impedance Spectra*, https://www.iam.kit.edu/et/english/Lin-KK.php.